Regolith grain sizes of Saturn's rings inferred from Cassini-CIRS far-infrared spectra

Ryuji Morishima[a,b,*], Scott G. Edgington[a], Linda Spilker[a]

[a]*Jet Propulsion Laboratory/California Institute of Technology, Pasadena, CA 91109, USA*
[b]*University of California, Los Angels, Institute of Geophysics and Planetary Physics, Los Angeles, CA 90095, USA*

Abstract

We analyze far-infrared (10-650 cm^{-1}) emissivity spectra of Saturn's main rings obtained by the Cassini Composite Infrared Spectrometer (CIRS). In modeling of the spectra, the single scattering albedos of regolith grains are calculated using the Mie theory, diffraction is removed with the delta-Eddington approximation, and the hemispherical emissivities of macroscopic free-floating ring particles are calculated using the Hapke's isotropic scattering model. Only pure crystalline water ice is considered and the size distribution of regolith grains is estimated. We find that good fits are obtained if the size distribution is broad ranging from 1 μm to 1-10 cm with a power law index of ~ 3. This means that the largest regolith grains are comparable to the smallest free-floating particles in size and that the power law indices for both free-floating particles and regolith grains are similar to each other. The apparent relative abundance of small grains increases with decreasing solar phase angle (or increasing mean temperature). This trend is particularly strong for the C ring and is probably caused by eclipse cooling in Saturn's shadow, which relatively suppresses warming up of grains larger than the thermal skin depth (~ 1 mm) under subsequent solar illumination.

Keywords: Saturn, Rings; Infrared observations; Radiative transfer; Regoliths

---

[*]Corresponding author
Email address: Ryuji.Morishima@jpl.nasa.gov (Ryuji Morishima)

1. Introduction

Saturn's rings consist of a large number of icy particles. The range of the particle size in the main rings (the A, B, C rings, and the Cassini division) deduced from radio and stellar light occultations is roughly 1 cm to 10 m (Marouf et al., 1983; Zebker et al., 1985; French and Nicholson, 2000; Cuzzi et al., 2009). The composition of ring particles is mostly crystalline water ice and the mass fraction of contaminants (e.g., Tholins, PAHs, or nanohematite) is ten percent at most (Epstein et al., 1984; Cuzzi et al., 2009) and probably less than one percent (Poulet et al., 2003). A favorable origin of Saturn's rings with such a high content of water ice is stripping of the icy mantle of a Titan-sized satellite (Canup, 2010). Subsequent meteoritic pollution for 4.5 Gyr may darken the rings too much if the ring mass has been kept similar to the present mass (Cuzzi and Estrada, 1998; Elliot and Esposito, 2011), but initially very massive rings suggested from the Canup's model have not yet been taken into account in pollution models.

Individual ring particles are likely to be covered by regolith grains [1], probably formed by meteoritic bombardment (Elliot and Esposito, 2011). The regolith grain size is estimated from ring spectra at different wavelengths from ultraviolet to submillimeter ranges, but the estimated size is puzzling as it increases with wavelength. For far-ultraviolet wavelengths, Bradley et al. (2010) estimate the mean photon path length, which is probably the order of the grain size, as 2-5 μm. For near-infrared wavelengths, the estimated grain size varies from author to author (Nicholson et al., 2008; Cuzzi et al., 2009[2]; Filacchione et al., 2012) ranging from 5 to 100 μm, but all these works suggest a relatively smaller size in the C ring than the A and B rings. These works for near-infrared spectra assume that the ring composition is pure water ice, and the size difference could be due to different water bands used or different radiative transfer models. Poulet et al. (2003) study the ring composition using both visible and near infrared spectra. Their model calls for a wide spread in grain sizes: 10-1000 μm for the A and B rings and 30-7500 μm for the C ring. The large difference in the grain size of the C ring from other works indicates that there is some degeneracy between the ring composition and grain size. For far-infrared wavelengths, Spilker et al.

---

[1] Throughout the paper, we use "particles" for free-floating particles and "grains" for regolith grains.

[2] A work by R. Clark in Cuzzi et al. (2009)

(2005) find that the B ring spectrum is well fitted by a model spectrum with the grain sizes ranging from 8 μm to 10 m and the power-law index of 3.4 (the upper limit of 10 m means that the entire ring is considered as regolith layers in their study).

Since Saturn orbit insertion of the Cassini spacecraft in July 2004, the Cassini Composite Infrared Spectrometer (CIRS) has obtained millions of spectra (7 μm - 1 mm) of Saturn's rings (Flasar et al., 2005; Spilker et al., 2005, 2006; Altobelli et al., 2007, 2008, 2009; Leyrat et al., 2008b; Flandes et al., 2010, Morishima et al., 2011). Except for Spilker et al. (2005), all above works discuss ring temperatures. The signal-to-noise levels of individual spectra are usually good enough to derive temperatures using Planck fits whereas averaging over many spectra are necessary for spectroscopy to examine grain sizes and possible contaminants. In Spilker et al. (2005), only the spectral data in the very early phase of the mission are analyzed. In the present study, using the many spectra we have obtained so far, radial variation and dependence on observational geometries are examined in detail.

In Section 2, we explain how to derive emissivity spectra from observed radiances. In Section 3, selection and averaging of data are discussed. In Section 4, the modeling of emissivity spectra is described. In Section 5, the estimated grain size distributions for different rings are shown. Interpretations of the results and comparison with previous works are discussed in Section 6. The summary of the present work is given in Section 7.

2. Derivation of emissivity spectra from observed radiances

The quantity directly obtained by the spectrometer is the radiance $I(\nu)$ as a function of wavenumber, ν. If the emissivity $\epsilon(\nu)$ is assumed not to vary over a footprint, the form of $I(\nu)$ for ring thermal emission is given as

$$I(\nu) = \epsilon(\nu)\beta_{\mathrm{geo}} \int f(T)B(T,\nu)dT, \tag{1}$$

where $\beta_{\mathrm{geo}}(\leq 1)$ is the geometric filling factor of a ring (see Sec. 2.4), $f(T)$ is the distribution function of temperature T inside a footprint, normalized as $\int f(T)dT = 1$, and $B(T,\nu)$ is the Planck function. Because the temperature inside the footprint is not known and may not be uniform, it is not straightforward to derive $\epsilon(\nu)$ from $I(\nu)$, unlike temperature-controlled laboratory measurements. With different assumptions, different types of emissivities are obtained. Three different emissivities are introduced in the following:

3

$\epsilon_0(\nu)$ derived by a fit with a single temperature, $\epsilon_1(\nu)$ derived by a fit with two temperatures, and $\epsilon_2(\nu)$ derived by a fit with two temperatures and an expected emissivity spectrum.

2.1. Fits with a single temperature

If the temperature distribution is represented by a single effective temperature T_0, one may have

$$\int f(T)B(T,\nu)dT = \beta_{\text{therm}}(\nu)B(T_0,\nu), \tag{2}$$

where β_{therm} is the correction factor due to multiple temperatures inside a footprint. The expected shape of β_{therm} is discussed in Sec. 2.2.

In the first method to obtain the emissivity is to assume $\beta_{\text{therm}}(\nu) = 1$. Substituting Eq. (2) into Eq. (1), we obtain

$$\epsilon_0(\nu) = \frac{I(\nu)}{\beta_{\text{geo}}B(T_0,\nu)}. \tag{3}$$

The temperature T_0 is obtained by minimizing the residuals R_0

$$R_0(T_0, \epsilon_{\text{sca},0}) = \sum_{\nu} \left(\frac{I(\nu) - \epsilon_{\text{sca},0}\beta_{\text{geo}}B(T_0,\nu)}{\sigma(\nu)} \right)^2, \tag{4}$$

where $\epsilon_{\text{sca},0}$ is the (scalar) emissivity averaged over wavelengths and $\sigma(\nu)$ is the instrument noise equivalent spectral radiance (NESR; see Flasar et al. 2004). The above Planck fits are applied to all CIRS ring spectra to obtain corresponding temperatures. In Spilker et al. (2005), Eqs. (3) and (4) are used and $\epsilon_0(\nu)$ is averaged over many spectra. Altobelli et al. (2008) estimated $\epsilon_{\text{sca},0}$ for the C ring to be ~ 0.9. It is expected that Eq. (4) works well if the temperature variation in the footprint is small ($\beta_{\text{therm}}(\nu) \simeq 1$) and $\epsilon(\nu)$ is roughly flat over wavelength of interest.

2.2. Fits with two temperatures

It is unlikely that the temperature inside a single footprint is perfectly uniform. The particle temperature may vary radially and vertically. Even on the surface of a single particle, large temperature variation may exist as the temperature is expected to be highest and lowest around the sub-solar and anti-sub-solar points, respectively. Instead of deriving a temperature

distribution with complicated thermal models which calculate the energy balance of rings, simply two portions with high and low temperatures (T_{w1} and T_{c1}) are considered:

$$\int f(T)B(T,\nu)dT = f_{w1}B(T_{w1},\nu) + (1 - f_{w1})B(T_{c1},\nu), \qquad (5)$$

where f_{w1} is the fraction of the warm portion. Fits with two temperatures are also used in analysis of thermal emission of icy satellites (Carvano et al. 2007; Howett et al. 2011). Substituting Eq. (5) into Eq. (1), the emissivity is given by

$$\epsilon_1(\nu) = \frac{I(\nu)}{\beta_{geo}\left[f_{w1}B(T_{w1},\nu) + (1 - f_{w1})B(T_{c1},\nu)\right]}. \qquad (6)$$

As in Eq. (4), the temperatures and factors are determined by minimizing the residual as

$$R_1(T_{w1}, T_{c1}, \epsilon_{sca,1}, f_{w1}) =$$
$$\sum_\nu \left(\frac{I(\nu) - \epsilon_{sca,1}\beta_{geo}\left[f_{w1}B(T_{w1},\nu) + (1 - f_{w1})B(T_{c1},\nu)\right]}{\sigma(\nu)}\right)^2, \qquad (7)$$

where $\epsilon_{sca,1}$ is the scalar emissivity. For the convenience of later use, we also define the relative emissivity $\epsilon_{rel,1}(\nu)$ as

$$\epsilon_{rel,1}(\nu) = \frac{\epsilon_1(\nu)}{\epsilon_{sca,1}}. \qquad (8)$$

The relative emissivity is roughly scaled to be unity, so is suitable for comparison between different spectra.

Equating Eqs. (2) and (5), the form of β_{therm} is given as

$$\beta_{therm}(\nu) = \frac{f_{w1}B(T_{w1},\nu) + (1 - f_{w1})B(T_{c1},\nu)}{B(T_0,\nu)}. \qquad (9)$$

An example of β_{therm} for various values of f_{w1} is shown in Fig. 1. Near the Planck peak (~ 200 cm^{-1}), β_{therm} takes the lowest value whereas β_{therm} is much larger than unity at large ν. Indeed most of spectra show large ϵ at large ν due to the effect of β_{therm}, if fits are done with a single Planck function.

2.3. Fits with two temperatures and an expected emissivity

The method in Sec. 2.2 works only if $\epsilon(\nu)$ is globally flat with possible narrow features in the wavenumber range of interest. If broad features exist, correct temperatures may not be retrieved. An extreme case is that $\epsilon(\nu)$ has a profile similar to $1/\beta_{\mathrm{therm}}(\nu)$. In this case, both $\epsilon(\nu)$ and $\beta_{\mathrm{therm}}(\nu)$ are incorrectly found to be nearly constant over the range of ν. In fact, we have this problem because $\epsilon(\nu)$ for water ice is an upward convex function around the Planck peak wavenumber for the ring temperature (Sec. 4). In this kind of situation, the temperatures (T_{w2} and T_{c2}) and the fraction of the warm portion (f_{w2}) may be retrieved with an expected (modeled) emissivity $\epsilon_{\mathrm{model}}(n_1, n_2, ..., \nu)$, where n_1, n_2, ... are parameters in models, as

$$R_2(T_{\mathrm{w2}}, T_{\mathrm{c2}}, f_{\mathrm{w2}}, n_1, n_2, ...) = \sum_{\nu} \left(\frac{I(\nu) - I_{\mathrm{model}}(T_{\mathrm{w2}}, T_{\mathrm{c2}}, f_{\mathrm{w2}}, n_1, n_2, ..., \nu)}{\sigma(\nu)} \right)^2 , \quad (10)$$

where

$$I_{\mathrm{model}}(T_{\mathrm{w2}}, T_{\mathrm{c2}}, f_{\mathrm{w2}}, n_1, n_2, ..., \nu) =$$
$$\epsilon_{\mathrm{model}}(n_1, n_2, ..., \nu)\beta_{\mathrm{geo}} \left[f_{\mathrm{w2}}B(T_{\mathrm{w2}}, \nu) + (1 - f_{\mathrm{w2}})B(T_{\mathrm{c2}}, \nu) \right]. \quad (11)$$

The retrieved emissivity is given as

$$\epsilon_2(\nu) = \frac{I(\nu)}{\beta_{\mathrm{geo}} \left[f_{\mathrm{w2}}B(T_{\mathrm{w2}}, \nu) + (1 - f_{\mathrm{w2}})B(T_{\mathrm{c2}}, \nu) \right]}. \quad (12)$$

It is expected that $\epsilon_{\mathrm{model}}(\nu)$ with best-fit parameters is close to $\epsilon_2(\nu)$.

In this study, we estimate best-fit values of model parameters using Eq. (10), rather than comparing $\epsilon_1(\nu)$ with $\epsilon_{\mathrm{model}}(\nu)$, because only poor fits are obtained for the latter case.

2.4. Geometric filling factor

The geometric filling factor β_{geo} is given as

$$\beta_{\mathrm{geo}}(B_{\mathrm{o}}) = 1 - \exp \left(-\frac{\tau(B_{\mathrm{o}})}{\sin |B_{\mathrm{o}}|} \right), \quad (13)$$

where B_{o} is the elevation angle of the observer and $\tau(B_{\mathrm{o}})$ is the normal optical depth of the ring. The optical depth τ is known to depend on B_{o} and also on longitude of the observer around the footprint relative to the

ring longitude because of wakes (Colwell et al., 2006, 2007, 2010; Hedman et al., 2007). In the present study, we only consider the B_o-dependence and $\tau(B_o)$ is obtained by interpolations using five τ profiles with different values of B_o (15.3, 21.1, 28.7, 54.0, and 66.7 degs). These data are available in Planetary Data System (Colwell et al., 2010). The τ profile for $B_o = 28.7$ degs is obtained by Voyager PPS while others are by Cassini UVIS. We interpolate τ if $\tau(B_o = 28.7$ degs$) < 0.2$ then convert it to β_{geo}, whereas β_{geo} is interpolated for larger τ. Usually τ has little dependence on B_o in regions with small τ. The interpolated profile of β_{geo} is smoothed over CIRS footprints (see Morishima et al., 2010).

3. Selection and averaging of data

Individual CIRS spectra are usually too noisy for spectroscopy and averaging over many spectra is necessary to reduce the noise level. Different types of averaging are considered. In previous works (Spilker et al., 2005; Carvano et al., 2007), the emissivities ($\epsilon_0(\nu)$ and $\epsilon_1(\nu)$) are averaged over after applying Planck fits to individual spectra. On the other hand, the radiance is averaged over and Planck fits are applied to the averaged spectra in this study. There are advantages and disadvantages in both methods. The latter method is numerically less intense than the former method, particularly if the number of parameters used in Planck fits are numerous like the case of $\epsilon_2(\nu)$. The channel-to-channel noise level is smaller for the latter method than the former method, as the noise originally arises in the radiance.

However, the following conditions are necessary for the latter method to work: (1) variation of the emissivity is small enough in the spectra used in an average, (2) correlation between $\beta_{therm}B(T,\nu)$ (temperature and its variation) and $\beta_{geo}(B_o)$ is small enough, and (3) temperature variation including both inside of individual footprints and over different footprints are still well approximated by a sum of two Planck functions. Averaging Eq. (1) over spectra, these conditions are represented as:

$$\begin{aligned}
\langle I(\nu)\rangle &= \epsilon_1(\nu)\langle\beta_{therm}(\nu)B(T,\nu)\beta_{geo}\rangle \\
&= \epsilon_1(\nu)\langle\beta_{therm}(\nu)B(T,\nu)\rangle\langle\beta_{geo}\rangle \\
&= \epsilon_1(\nu)\left[f_{w1}B(T_{w1},\nu) + (1-f_{w1})B(T_{c1},\nu)\right]\langle\beta_{geo}\rangle.
\end{aligned} \quad (14)$$

A similar equation is also obtained for $\epsilon_2(\nu)$.

In order to check whether these conditions are fulfilled, we test various types of grouping of spectra based on saturnocentric radius, observational

geometry, and temperature, T_0, while keeping a certain number of spectra in a parameter bin for a good signal-to-noise level. After many trials, we divide spectra into six radial bins (the inner and outer C ring, inner and outer B ring, Cassini division, and A ring) and into temperature (T_0) bins with the interval of 5 K. These bins are chosen because apparent spectral shapes depend on saturnocentric radius and temperature. The temperature dependence probably represents the dependence on observational geometries. Noise cancellation works better with temperature bins rather than using bins of geometric parameters, and also an unnecessary enhancement of the effect of β_{therm} is suppressed by averaging spectra with similar temperatures. We do not divide spectra by B_{o} because we find that there is only small difference between averaged spectra at high and low $|B_{\mathrm{o}}|$, provided that other conditions are the same. This means that the condition (2) is almost fulfilled. The number of spectra in the bins, the mean solar phase angle, and the mean absolute solar elevation angles are shown in Fig. 2. The highest temperature is obtained at low phase angle and at high solar elevation, while the temperature decreases with decreasing solar elevation and increasing phase angles.

The above binning is made for all spectra obtained until the end of 2010 after removing very noisy spectra. We only analyze spectra in the far-infrared channel (focal plane 1; 10 cm^{-1} < ν < 650 cm^{-1}) with $T_0 \geq 70$ K, as spectra at low temperatures or in the mid-infrared channel (focal planes 3 and 4; 600 cm^{-1} < ν < 1400cm^{-1}) are too noisy even after averaging. We only show spectral data at the lowest spectral resolution, 15.5 cm^{-1} (the interpolated spectral step is 5 cm^{-1}), in this paper. Spectra with higher resolutions are noisier but show good agreement with the lowest resolution data in most cases.

Examples of the relative emissivity $\epsilon_{\mathrm{rel},1}(\nu)$ for different temperatures T_0 are shown in Figs. 3 and 4 for the inner C ring and the outer B ring, respectively. The emissivity spectra for the inner C ring show strong dependence on temperature whereas the inner B ring spectra show little dependence on temperature. These temperature dependence and independence are also confirmed in higher spectral resolution data. The dip seen at 230 cm^{-1} (clearly seen in Fig. 4 but ambiguous in Fig. 3) is a feature caused by intermolecular vibrations (transverse-optical mode) of water ice. Other narrow features are

noises specific to the CIRS instrument (Carlson et al. 2009[3]): the real-time interrupt (RTI) noise (191, 383, and 574 cm^{-1}) and a prominent single frequency (sine wave in interferograms) feature of unknown origin that has been observed between 18 cm^{-1} and 210 cm^{-1} (seen at 80 cm^{-1} in Fig. 3 and at 150 cm^{-1} in Fig. 4). The noise level is not shown in Figs. 3 and 4, but the channel-to-channel noise level is expected to be $\sim \sigma(\nu)/(\langle \beta_{\mathrm{geo}} \rangle B(T_0, \nu) N_{\mathrm{spec}}^{1/2})$ and is small enough due to large N_{spec}, except at the wave numbers of the CIRS specific noise. The standard deviation of the radiance in spectral averaging is not used, as it is independent of N_{spec} and makes formal error bars artificially large (Clark et al., 2008). Most of the spectra in Figs. 3 and 4 show increase of $\epsilon_{\mathrm{rel},1}(\nu)$ with ν for $\nu > 400$ cm^{-1}. This is due to the effect of β_{therm} which is not removed appropriately even with two temperature fits. This artificial effect will be better corrected in $\epsilon_2(\nu)$.

4. Emissivity modeling

In our emissivity model, the single scattering albedos of regolith grains are calculated using the Mie theory (Mie, 1908; Bohren and Huffman, 1983), diffraction is removed with the delta-Eddington approximation (Joseph et al., 1974), and the hemispherical emissivities for macroscopic particles are calculated using the Hapke's isotropic scattering model (Hapke, 1993). Cheng et al. (2010) compare the mid-infrared emissivity spectra (8-13 μm) of snow surfaces obtained by field measurements of Hori et al. (2006) with those from various types of emissivity models, and find that the Mie-Hapke hybrid model with diffraction removal is the best choice. The Mie-Hapke hybrid model is also the best choice for emissivity modeling of quartz (Moersch and Christensen, 1995) and olivine (Mustard and Hays, 1997), although diffraction removal does not improve fits for quartz (Pitman et al., 2005).

The Mie theory calculates absorption and scattering of a sphere with a given size parameter $X = 2\pi r/\lambda$ (where r is the grain radius and λ is the wavelength of incident wave) and the real and imaginary parts of the refractive indices, n and k. In the present work, we only consider pure crystalline water ice. To date non-water ices (NH_3, CO_2, and CH_4) have not yet been

---

[3]De-spiking of interferograms described in Carlson et al. (2009) has not been applied to the 15.5 cm^{-1} data. See also "Interferences on CIRS interferograms and spectra: A user guide" by Nixon et al. at http://pds-rings.seti.org/vol/COCIRS_0409/DOCUMENT/cirs_interferences.pdf.

identified in CIRS far-infrared spectra (Edgington et al., 2008), and effects of possible contaminants will be examined more in detail in future work. The refractive indices of crystalline water ice used for the Mie calculations are shown in Fig. 5. We use n and k at 136 K from Curtis et al. (2005) for 50 cm^{-1} < ν < 650cm^{-1} and k at 90 K from the theoretical fitting function of Mishima et al. (1983) for 10 cm^{-1} < ν < 30 cm^{-1}. We assume that n is constant for ν < 50 cm^{-1}, and $\log k$ is linearly interpolated between 30 and 50 cm^{-1}. The temperature of Saturn's rings is lower than 136 K, but no good data are available at ring temperatures for crystalline water ice. The refractive indices weakly depend on temperature, particularly, ν at the peak of k (near 230 cm^{-1}) weakly increases with decreasing temperature (Curtis et al., 2005). In fact, the CIRS emissivity spectra show the peak wavenumber slightly larger than the model prediction (see Fig. 8), as we use n and k at the warmer temperature. The samples of Curtis et al. (2005) at temperatures lower than 136 K are amorphous and amorphous ice shows ν at the peak of k slightly lower than that for crystalline ice (Fig. 5). This indicates that Saturn's rings most likely consist of crystalline ice. The same conclusion is also derived from the Fresnel peak position in near-infrared spectra (Cuzzi et al., 2009).

Using the extinction efficiency Q_{ext0} and the scattering efficiency Q_{sca0} from the Mie theory, the single scattering albedo ω_0 is given as

$$\omega_0 = \frac{Q_{\mathrm{sca0}}}{Q_{\mathrm{ext0}}}. \tag{15}$$

Figure 6a shows Q_{ext0} and ω_0 for various grain radii. In the Mie theory, scattered light includes diffracted light. In a closely packed medium, however, inter-grain spaces are narrow so that the diffracted light is suppressed (Hapke, 1999). Different methods of diffraction removal are proposed (Joseph et al., 1976; Wiscombe, 1977; Mishchenko, 1994; Wald, 1994) and we apply the delta-Eddington approximation proposed by Joseph et al. (1976) because of its convenience. In this approximation, the diffraction is approximated by a forward-scattering delta function and its contribution is calculated by assuming that the second moment of the sum of the delta function and the diffraction-removed phase function is identical to that for the original phase function. The extinction efficiency Q_{ext}, the scattering efficiency Q_{sca}, and the single scattering albedo, ω, after diffraction removal are given as

$$Q_{\mathrm{ext}} = (1 - \omega_0 g_0^2) Q_{\mathrm{ext0}}, \tag{16}$$

10

$$Q_{\text{sca}} = (1 - g_0^2)\omega_0 Q_{\text{sca0}}, \qquad (17)$$

$$\omega = \frac{Q_{\text{sca}}}{Q_{\text{ext}}}, \qquad (18)$$

where g_0 is the anisotropic parameter calculated by the Mie-theory. Figure 6b shows Q_{ext} and ω for same grain sizes used in Fig. 6a. It is found that ω is usually much lower than ω_0. For $X \gg 1$, $Q_{\text{ext0}} \simeq 2$ whereas $Q_{\text{ext}} \simeq 1$, as expected. The Mie parameters are little affected by the delta-Eddington approximation for small grains ($X < 1$), because g_0 approaches zero in the Rayleigh scattering regime. However, differences in ω due to different diffraction subtraction methods are large for small grains (not shown). Fortunately, this has little impact if a broad size distribution including large grains is taken into account, because Q_{ext} for small grains is so small that its contribution to scattering is reduced (see Eq. (19)). The exception is near the peak of k at 230 cm^{-1}, where Q_{ext} is large even for $X < 1$, and there is little difference between Q_{ext0} and Q_{ext}, even applying any diffraction subtraction method.

For a size distribution, the single scattering albedo is effectively given as

$$\omega = \frac{\int \pi r^2 Q_{\text{sca}}(r) n(r) dr}{\int \pi r^2 Q_{\text{ext}}(r) n(r) dr}. \qquad (19)$$

We assume the number of grains per unit radius is given by a power-law

$$n(r) = n_0 \left(\frac{r}{r_0}\right)^{-p}, \qquad (20)$$

where p is the index, n_0 and r_0 are constants. The black thin lines in Fig. 6a and 6b show ω_0 and ω for $p = 3$ with the minimum and maximum cut-off sizes of $r_{\text{min}} = 1$ μm and $r_{\text{max}} = 1$ cm. The logarithmic bins with an increment of $2^{1/4}$ are used for r.

Hapke (1993) derives analytic expressions of various types of reflectances and emittances using the two stream approximation for isotropic scattering grains. Using ω, the Bond (spherical) albedo of a macroscopic ring particle comprised of regolith grains is given as (Eq. (10.51b) of Hapke, 1993)

$$A_{\text{BOND}} = \frac{1 - \gamma}{1 + \gamma} \left(1 - \frac{1}{3} \frac{\gamma}{1 + \gamma}\right), \qquad (21)$$

with

$$\gamma = \sqrt{1 - \omega}. \qquad (22)$$

11

Finally, the hemispherical emissivity ϵ_{model} of the ring particle is given from the Kirchhoff's law as (Eq. (13.29) of Hapke, 1993)

$$\epsilon_{\text{model}} = 1 - A_{\text{BOND}}. \tag{23}$$

For spatially resolved planetary or satellite surfaces, the directional emissivity is usually used, whereas we use the hemispherical emissivity (the hemispherically averaged directional emissivity) as we see thermal emission from entire hemispheres of ring particles. We only considered intra-particle regolith radiative transfer, ignoring inter-particle scattering. Indirect evidence that inter-particle scattering is unimportant is obtained from a similarity of the emissivity spectra between the B and A rings despite the optical depth difference between them (see Sec. 5 for a more detailed discussion).

Bottom panels of Figs. 6a and 6b show ϵ_{model} without and with diffraction removal. For large grains ($r > 100$ μm), the overall profile of ϵ_{model} is flat down to ~ 50 cm^{-1}, and a spectral roll-off is seen for lower ν; the exact value of ν below which a roll-off is seen decreases with increasing r. The location of a roll-off seen in CIRS spectra (Figs. 3 and 4) indicates that large grains indeed exist in regoliths of Saturn's rings. The prominent dip of ϵ_{model} corresponding to the k peak is seen at 230 cm^{-1}, and ϵ_{model} is slightly larger for > 230 cm^{-1} than for < 230 cm^{-1} (for example, compare values at 170 cm^{-1} and 280 cm^{-1}). Intermediate-sized grains (10 μm $< r < 100$ μm) show a broad hump between 100 cm^{-1} and 300 cm^{-1} due to inter-molecular vibrations of water ice. The hump features are also seen in many CIRS spectra. The emissivity of small grains ($r < 10$ μm) are almost unity for < 300 cm^{-1}, because they behave as Rayleigh absorbers. Their extinction efficiencies are high only near 230 cm^{-1} so that they reduce the depth of the dip at 230 cm^{-1} produced by large grains.

The one issue we find in emissivity fits is that a large amount of small grains is necessary to produce the shallow 230 cm^{-1} feature seen in CIRS spectra whereas too large a fraction of small grains makes entire fits worse. An alternative way to reduce the depth of the 230 cm^{-1} feature instead of adding too many small grains is to introduce intra-grain pores. If the pore size is sufficiently smaller than the wavelength, the complex permittivity, $K(\phi) = (n^2 - k^2) + i(2nk)$, as a function of the porosity ϕ is given from the Maxwell-Garnett theory (Maxwell-Garnett, 1904) as

$$K(\phi) = K(0) \left(1 + \frac{3\phi(1 - K(0))}{1 + 2K(0) - \phi(1 - K(0))} \right). \tag{24}$$

12

The validity of this equation is confirmed by laboratory measurements of silicon (Labbé-Lavigne et al., 1998). The refractive indices for $\phi = 0.5$ are shown in Fig. 5. Figure 6c shows Q_{ext}, ω, and $\epsilon_{\mathrm{model}}$ for $\phi = 0.5$ and with diffraction removal. It is found that the overall shape of $\epsilon_{\mathrm{model}}$ in Fig. 6c is similar to that in Fig. 6b except the depth of the 230 cm^{-1} feature is shallower with intra-grain pores. Since introducing intra-grain pores has an effect similar to reducing grain-size, the estimated grain size effectively increases, but the change in estimated size is very small as long as $\phi \leq 0.5$.

5. Estimated regolith size

The best-fit values of model parameters are estimated from Eq. (10). In the model fits, we fix the minimum grain size and intra-grain porosity at $r_{\mathrm{min}} = 1$ μm and $\phi = 0.5$ and seek the best-fit values of the maximum size r_{max} and the power-law index p. The reason for choosing $r_{\mathrm{min}} = 1$ μm is that existence of micron-sized grains is supported from the grain size of spokes ($r \sim 2$ μm; D'aversa et al., 2010) and from UVIS spectra ($r \sim 2$-5 μm; Bradley et al., 2010). We do not examine cases with r_{max} larger than 1 m because this is a typical size of large free-floating particles (French and Nicholson, 2000).

The residual R_2 is calculated as a function of r_{max} and p, each pair of r_{max} and p having the optimal temperatures and the fraction of the warm portion. We introduce the normalized residual:

$$\tilde{R}_2(p, r_{\mathrm{max}}) = \frac{R_2}{R_{2,\mathrm{min}}} - 1, \tag{25}$$

where $R_{2,\mathrm{min}}$ is the minimum value of R_2 in the parameter space. Some examples of $\tilde{R}_2$ on the r_{max} vs. p plane are shown in Fig. 7. The error bars for r_{max} and p are estimated from the maximum and minimum values of these parameters on the curve of $\tilde{R}_2 = 1$. It is found that p can be constrained in some ranges whereas only the lower limit of r_{max} (3-10 mm for cases in Fig. 7) is well constrained.

Some examples of the best-fit spectrum, $\epsilon_{\mathrm{model}}$, are shown together with ϵ_2 and ϵ_1 in Fig. 8. Note that ϵ_2 and ϵ_1 are obtained from the same radiance data and the difference comes from the fitted temperatures and the fraction of the warm portion (Sections 2.2 and 2.3). Good agreements between $\epsilon_{\mathrm{model}}$ and ϵ_2 are obtained for all cases at least for $\nu < 300$ cm^{-1} and sometimes over all the wavenumber range. On the other hand, the absolute value of ϵ_1

13

is much lower than $\epsilon_{\mathrm{model}}$ with any grain sizes. In addition to that, ϵ_1 for $\nu \sim 170$ cm^{-1} is comparable to or higher than ϵ_1 for $\nu \sim 280$ cm^{-1} whereas the opposite trend is seen for $\epsilon_{\mathrm{model}}$. The temperature $T_{\mathrm{c}2}$ is found to be always lower than $T_{\mathrm{c}1}$. With decreasing temperature from $T_{\mathrm{c}1}$ to $T_{\mathrm{c}2}$, the absolute value of ϵ increases in all wavenumbers and the overall slope $d\epsilon/d\nu$ increases. Consequently, ϵ_2 for $\nu \sim 280$ cm^{-1} can be larger than that for $\nu \sim 170$ cm^{-1} as is the case of pure water ice. Although lowering only the temperature of the cold portion makes ϵ at large ν (typically > 400 cm^{-1}) larger than unity, ϵ in this region is reduced by increasing the temperature and fraction of the warm portion (note $f_{\mathrm{w}2} > f_{\mathrm{w}1}$ or/and $T_{\mathrm{w}2} > T_{\mathrm{w}1}$ in all cases). Some cases shows only one temperature component ($f_{\mathrm{w}1} = 0$) for the derivation of ϵ_1 (e.g., the C ring data in Fig. 8), but existence of two temperature components, as is the case for ϵ_2, is also physically reasonable considering a possible temperature variation over the surfaces of ring particles.

Figure 9 shows the summary of estimated values of p and r_{max} for all cases. It is found that $p \simeq 3$ for most of the cases (Fig. 9a) except that the C ring shows slightly larger values and the Cassini division shows slightly smaller values at high temperatures. Interestingly, the values of p are quite close to those for macroscopic particles (French and Nicholson, 2000). The maximum size r_{max} is estimated to be 1-100 cm in most of cases. The lower limit of r_{max} is well constrained, and in almost all cases r_{max} is larger than 1 mm (Fig. 9b). On the other hand, the upper limit of r_{max} is not well constrained from our data. However, r_{max} is expected to be smaller than the size of large particles ~ 1 m at least by an order of magnitude and probably even smaller in the following reasons. First, the total cross sections of any particles are equal in logarithmic bins for $p = 3$, and thus the broad size distribution we obtained means that the surface of a free-floating particle is not occupied by the largest regolith grains. Second, if inter-grain scattering is less than that expected from the radiative transfer model due to large grains comparable to the particle in size, the emissivity spectra may become closer to $1 - \omega$ instead of $1 - A_{\mathrm{Bond}}$. This clearly makes our fits worse; in particular, the depth of the 230 cm^{-1} feature will be too deep. Most likely, r_{max} is ~ 1 - 10 cm. This means that the largest regolith grains are comparable to the smallest free-floating particles in size. It is likely that grains smaller than 1-10 cm adhesively stick to large particles due to the surface energy (Bodrova et al., 2012), while larger grains are cores of particles hidden under smaller grains, if they exists.

The A and B rings show quite similar values of p and r_{max}. In addition

14

to that, these rings show very similar depths of the 230 cm^{-1} feature. If the optical depth of a ring is large enough and inter-particle scattering occurs, the emissivity of the ring may be calculated from Eqs. (21) and (23) assuming that the single scattering albedo is now given as the Bond albedo of ring particles. The resulting ring emissivity should have a shallower depth of the 230 cm^{-1} feature as compared with that without inter-particle scattering, from comparison of the depths for $1-\omega$ and $\epsilon_{\mathrm{model}}$ in Fig. 6b or 6c. Therefore, if regolith sizes are the same and inter-particle scattering is important, the depth of the 230 cm^{-1} feature is expected to decrease with increasing optical depth; such a correlation is not seen in spectra ($\tau \sim 2$ for the outer B ring while $\tau \sim 0.5$ for the A ring). Therefore, inter-particle scattering of far-infrared light is likely to be negligible. Little inter-particle scattering in near-infrared light is also suggested at low phase angles (Cuzzi et al., 2009).

The observed spectra for the C ring at low temperatures or the Cassini division do not clearly show the 230 cm^{-1} feature in contrast to the modeled ones. Higher spectral resolution data (not shown) seem to show that the feature actually exists both for the C ring and the Cassini division but it is narrower and shallower than that for the A and B rings (see also Figs. 3 and 4). What causes the feature less evident is unclear. It may be due to low signal-to-noise ratios for the optically thin rings, to intra-grain porosities higher than we assume (0.5), or to effects of contaminants including amorphous water ice. Since higher spectral resolution data are noisy, more careful analysis is necessary.

6. Discussion

6.1. Dependence of size distribution on temperature

What causes the dependence of size distribution on temperature seen in Fig. 9? This is probably caused by effects of observational geometries in conjunction with non-uniform temperature distribution of ring particles over surfaces and depth. If the temperature of a ring particle is completely uniform, it is expected that the emissivity spectrum of the particle is independent of observational geometry. However, in actual rings, the strongest thermal emission comes from near the subsolar points (seen at low solar phase angles) of slowly rotating particles at high solar elevation angles. In addition to that, due to eclipse cooling in Saturn's shadow, the strongest emission comes from only a thin surface layer with a thickness given by the thermal skin depth ℓ. If the thermal inertia is ~ 10 Jm^{-2}K^{-1}s$^{-1/2}$ as estimated by

15

Ferrari et al. (2005) and Morishima et al. (2011), $\ell \sim 1$ mm (e.g., Morishima et al., 2009). This is smaller than the size of the largest regolith grains estimated in Sec. 5. Therefore, the largest grains are only partially heated or their temperatures are lower than small grains near the subsolar point. As a result, thermal emission from the largest grains is suppressed relative to that from small grains at high temperatures. At higher solar phase angles and at lower solar elevation angles, variation of the particle temperature with depth is much smaller so that large grains can have temperatures similar to those for small grains. The dependence of size distribution on temperature is seen most strongly in the C ring, probably because the periodic temperature variation due to eclipse cooling is particularly large for the C ring as it is close to Saturn (long duration in the shadow) and has low photometric albedo (high temperature outside the shadow).

To reinforce the above discussion, let us estimate the depth from which thermal emission comes. The electric skin depth may be simply given by a depth where the optical depth of regolith layers is unity, unless grains are highly reflecting. The regolith optical depth as a function of depth is given as

$$\tau(z) = z \int_{r_{\min}}^{r_{\max}} \pi r^2 Q_{\text{ext}}(r, \nu) n(r) dr, \qquad (26)$$

where n is the particle number density per unit volume and per unit size. The number density n is defined by the following equation:

$$1 - \phi_{\text{inter}} = \int_{r_{\min}}^{r_{\max}} \frac{4}{3} \pi r^3 n(r) dr, \qquad (27)$$

where ϕ_{inter} is the inter-grain porosity. Using these equations, the electric skin depth is given as

$$z(\tau = 1) = \frac{3 r_{\text{eff}}}{4 Q_{\text{ext,eff}} (1 - \phi_{\text{inter}})}, \qquad (28)$$

where the effective grain radius r_{eff} and the effective extinction efficiency $Q_{\text{ext,eff}}$ are given by

$$r_{\text{eff}} = \frac{\int_{r_{\min}}^{r_{\max}} \pi r^3 n(r) dr}{\int_{r_{\min}}^{r_{\max}} \pi r^2 n(r) dr}, \qquad (29)$$

and

$$Q_{\text{ext,eff}}(\nu) = \frac{\int_{r_{\min}}^{r_{\max}} \pi r^2 Q_{\text{ext}}(r, \nu) n(r) dr}{\int_{r_{\min}}^{r_{\max}} \pi r^2 n(r) dr}. \qquad (30)$$

16

Since $Q_{\text{ext,eff}}(\nu)$ is $\sim$ 0.5-1.0, $z(\tau = 1)$ is larger than r_{eff} by a factor of 2-3, unless ϕ_{inter} is close to unity. Figure 10a shows r_{eff} estimated from p and r_{max} from Fig. 9. It is found that r_{eff} is $\sim$ 1 mm ($\sim \ell$) at the highest temperatures and is one or two orders of magnitude larger for lower temperatures. This indicates that if the temperature is uniform as is likely to be the case at low temperatures, thermal emission come from 1-10 cm in depth. However, thermal emission at the highest temperatures comes from a surface layer of 1 mm because only the thin layer is heated to the the highest temperature and emission from deeper and colder layers contribute much less to the total emission from the surface.

6.2. Comparison with grain sizes estimated in previous works

It is not straightforward to compare the size distribution estimated from the present work and those from other works, because other works usually consider single sizes or a few discrete sizes. If spectral behavior is monotonically dependent on grain size, a spectrum for a broad size distribution may be similar to the one for the median grain radius r_{med}, which is defined so that the total cross section of particles with $r > r_{\text{med}}$ is equal to that with $r < r_{\text{med}}$:

$$\int_{r_{\text{med}}}^{r_{\text{max}}} \pi r^2 n(r) dr = \frac{1}{2} \int_{r_{\text{min}}}^{r_{\text{max}}} \pi r^2 n(r) dr. \tag{31}$$

Figure 10b shows r_{med}. For the C ring, r_{med} strongly depends on temperature, but as we discussed in Sec. 6.1, the relative fraction of small grains are likely to be overestimated at high temperatures. Therefore, r_{med} is typically a few hundred microns or larger for all rings.

The mean photon path length (2-5 μm) estimated from far-ultraviolet spectra (Bradley et al., 2010) is clearly much smaller than r_{med}. The path length probably represents the size of cracks or flaws inside large grains or represents the smallest grain size, as suggested by Bradley et al. (2010). The typical value of r_{med} seems to be also larger than the grain sizes ($\leq$ 100 μm) estimated from the water band depths in near-infrared wavelengths (Nicholson et al., 2008; Cuzzi et al., 2009; Filacchione et al., 2012). It is cautioned that this comparison is not very precise, as some of the water band depths do not depend on particle size monotonically (see Fig. 15.27 of Cuzzi et al. (2009)). Nevertheless, some other bands show rather monotonic dependences on size (up to $\sim$ 1-10 cm) and the estimated sizes from these bands are still smaller than 100 μm. This size is probably underestimated as discussed in the following.

The grain sizes of snow on Earth are also estimated from reflectances in different bands in visible and near-infrared wavelengths and the estimated sizes are compared with the sizes from in-situ measurements. Some works (Fily et al., 1997; Aoki et al., 2007; Kuchiki et al., 2009) find that the grain sizes estimated from the 1.6 μm band, which is in one of the water absorption bands, are underestimated. Kuchiki et al. (2009) find that the grain size is underestimated when the actual grain size is large (> 1 mm) and point out that it is probably caused by microstructures on large grains' surfaces. It is plausible that regolith grains in ring particles are also not spheres but have surface microstructures. If it is the case, it may not be very appropriate to estimate the sizes of large grains from the water band depths, whereas spectral roll-offs at long wavelengths seen in CIRS spectra are likely to be less affected by microstructures. The large C ring grain sizes (30-7500 μm, which gives $r_{\mathrm{med}} \sim 1$ mm) estimated from spectra in the entire visible and near-infrared wavelength range (Poulet et al., 2003) look consistent with our results.

7. Summary

In this study, the far-infrared emissivity spectra of Saturn's main rings obtained by Cassini CIRS are analyzed. Ring spectra are divided into six radial bins and temperature bins with the width of 5 K, and the radiances are averaged over bins to reduce the noise levels. The temperatures and size distribution of regolith grains are simultaneously retrieved by the chi-square fits, provided that ring particles are composed of pure water ice. In modeling, the Mie-Hapke hybrid model is used with diffraction removal. Good fits are obtained if size distribution is broad ranging from 1 μm to 1-10 cm with the power law index of ~ 3. This means that the largest regolith grains are comparable to the smallest free-floating particles in size and that the power law indices for both free-floating particles and regolith grains are similar to each other.

The apparent relative abundance of small grains increases with decreasing phase angle (or increasing mean temperature). This trend is particularly strong for the C ring and is probably caused by eclipse cooling in Saturn's shadow, which relatively suppresses warming up of grains larger than the thermal skin depth (~ 1 mm) under subsequent solar illumination. The A and B ring spectra are found to be very similar to each other despite the

difference in optical depth, and this probably indicates that there is little scattering of far-infrared light between free-floating macroscopic particles.

There are a lot of things to do in future work. Effects of possible contaminants need to be investigated. Since the imaginary part of the refractive indices for water ice is high in the broad range of far-infrared wavelengths, effects of contaminants are probably small if they are mixed as small inclusions ($r \ll \lambda$) inside grains. Nevertheless, some possible contaminants, such as SiO_2, Fe_2O_3, NH_3, and NaCl, have strong absorption peaks in the CIRS wavelength region, and the upper limits of their abundances may be well constrained even if they are not identified. The effects of contaminants are probably more important if they are intimately mixed ($r > \lambda$). One of plausibly intimately-mixed contaminants is amorphous carbon (Poulet et al., 2003). It is also necessary to reduce CIRS specific noises with better calibration. Use of high spectral resolution data may also help improve model fits. The accurate determination of refractive indices of crystalline water ice at low ring temperatures (< 100 K) are also needed.

Acknowledgements

REFERENCES

Aoki, T. et al., 2007. ADEOS-II/GLI snow/ice products - Part II: Validation results using GLI and MODIS data. Remote Sens. Environ. 111, 274–290

Altobelli, N., Spilker, L.J., Pilorz, S., Brooks, S., Edgington, S., Wallis, B., Flasar, M., 2007. C ring fine structures revealed in the thermal infrared. Icarus 191, 691–701.

Altobelli, N., Spilker, L.J., Leyrat, C., Pilorz, S., 2008. Thermal observations of Saturn's main rings by Cassini CIRS: Phase, emission and solar elevation dependence. Planet. Space. Sci. 56, 134–146.

Altobelli, N., Spilker, L.J., Pilorz, S., Leyrat, C., Edgington, S., Wallis, B., Flandes, A., 2009. Thermal phase curves observed in Saturn's main rings by Cassini-CIRS: Detection of an opposition effect? Geophys. Res. Lett. 36, L10105.

Bodrova, A., Schmidt, J., Spahn, F., Brilliantov, N., 2012. Adhesion and collisional release of particles in dense planetary rings. Icarus 218, 60–68.

Bohren, C.F., Huffman, D.R., 1983. Absorption and scattering of light by small particles. Wiley, New York.

Bradley, E.T. Colwell, J.E., Esposito, L.W., Cuzzi, J.N., Tollerud, H., Chambers, L., 2010. Far ultraviolet spectral properties of Saturn's rings from Cassini UVIS. Icarus 206, 458–466.

Canup, R., 2010. Origin of Saturn's rings and inner moons by mass removal from a lost Titan-sized satellite. Nature 468, 943–946.

Carlson, R.C., Guandique, E.A., Jennings, D.E., Pilorz, S.H., Kunde, V.G., 2009. Characterization and suppression of electrical interference - spikes, periodic waves, and ripples - from Cassini Composite Infrared Spectrometer (CIRS) Spectra. FTS for Astronomy and Astrophysics, FtuA5.

Carvano, J.M., Migliorini, A., Barucci, A., Segura, M., the CIRS team, 2007. Constraining the surface properties of Saturn's icy moons, using Cassini/CIRS emissivity spectra. Icarus 187, 574–583.

Cheng, J., Liang, S., Weng, F., Wang, J., Li, X., 2010. Comparison of radiative transfer models for simulating snow surface thermal infrared emissivity. IEEE Journal of Selected Topics in Applied Earth Observations and Remote Sensing, 323–336.

Clark, R.N. et al., 2008. Compositional mapping of Saturns satellite Dione with Cassini VIMS and implications of dark material in the Saturn system. Icarus 193, 372–386.

Colwell, J.E., Esposito, L.W., Sremčević, M., 2006. Self-gravity wakes in Saturn's A ring measured by stellar occultations from Cassini. Geophys. Res. Lett. 33, L07201.

Colwell, J.E., Esposito, L.W., Sremčević, M., Stewart, G.R., McClintock, W.E., 2007. Self-gravity wakes and radial structure of Saturn's B ring. Icarus, 190, 127–144.

Colwell, J.E., Esposito, L.W., Jerousek, R.J., Sremčević, M., Pettis, D., Bradley, E.T., 2010. Cassini UVIS stellar occultation observations of Saturn's rings. Astron. J. 140, 1569–1578.

Curtis, D.B., Rajaram, B., Toon, O.B., Tolbert, M.A., 2005. Measurement of the temperature-dependent optical constants of water ice in the 15-200 μm range. Appl. Opt. 44, 4102–4118.

Cuzzi, J. N., Estrada, P.R., 1998. Compositional evolution of Saturn's rings due to meteoroid bombardment. Icarus 132, 1–35.

Cuzzi, J.N., Clark, K., Filacchione, G., French, R., Jhonson, R., Marouf, E., Spilker, L., 2009. Ring particle composition and size distribution. In: Dougherty, M.K., Esposito, L.W., Krimigis, S.M. (Eds.), Saturn from Cassini-Huygens. Springer, Berlin, pp. 459–509.

D'Aversa, E., Bellucci, G., Nicholson, P.D., Hedman, M.M., Brown, R.H., Showalter, M.R., Altieri, F., Carrozzo, F.G., Filacchione, G., Tosi, F., 2010. The spectrum of a Saturn ring spoke from Cassini/VIMS. Geophys. Res. L. 37, L01203.

Elliott, J.P., Esposito, L.W., 2011. Regolith depth growth on an icy body orbiting Saturn and evolution of bidirectional reflectance due to surface composition changes. Icarus 212, 268–274.

Edgington, S.G., Spilker, L.J., Leyrat, C., Nugent, C.R., Jennings, D.E., Pilorz, S.H., Pearl, J.C., and the CIRS team, 2008. Emissivity in the thermal IR: Composition and polarization in Saturn's rings with Cassini/CIRS. Bulletin of the American Astronomical Society 40, 443

Epstein, E.E., Jamssem, M.A., Cuzzi, J.N., 1984. Saturn's rings: 3-mm low inclination observations and derived properties.

Ferrari, C., Galdemard, P., Lagage, P.O., Pantin, E., Quoirin, C., 2005. Imaging Saturn's rings with CAMIRAS: thermal inertia of B and C rings. Astron. Astrophys. 441, 379–389.

Filacchione, G., et al., 2012. Saturn's icy satellites and rings investigated by Cassini-VIMS III: Radial compositional variability. Icarus 220, 1064–1096.

Fily, M., Bourdelles, B., Dedieu, J.P., Sergent, C., 1997. Comparison of in situ and Landsat Thematic Mapper derived snow grain characteristics in the Alps. Remote Sens. Environ. 59, 452–460.

Flandes, A., Spilker, L.J., Morishima, R., Pilorz, S., Leyrat, C., Altobelli, N., Brooks, S.M., Edgington, S.G., 2010. Brightness of Saturn's rings with decreasing solar elevation. Planet. Space Sci. 58, 1758–1765.

Flasar, F.M. et al., 2004. Exploring the Saturn system in the thermal infrared: The composite infrared spectrometer. Space Sci. Rev. 115, 169–297.

Flasar, F.M. et al., 2005. Temperatures, winds, and composition in the Saturnian system. Science 307, 1247–1251.

French, R.G., Nicholson, P.D., 2000. Saturn's rings II. Particle sizes inferred from stellar occultation data. Icarus 145, 502–523.

Hapke, B., 1993. Theory of reflectance and emittance spectroscopy. Cambridge Univ. Press, New York.

Hapke, B., 1999. Scattering and diffraction of light by particles in planetary regoliths. J. Quant. Spectrosc. Radiat. Transfer 61, 565–581.

Hedman, M.M., Nicholson, P.D., Salo, H., Wallis, B.D., Buratti, B.J., Baines, K.H., Brown, R.H., Clark, R.N., 2007. Self-gravity wake structures in Saturn's A ring revealed by Cassini VIMS. Astron. J. 133, 2624–2629.

Hori, M. et al., 2006. In-situ measured spectral directional emissivity of snow and ice in the 8–14 μm atmospheric window. Remote Sens. Environ. 100, 486–502.

Howett, C.J.A., Spencer, J.R., Pearl, J., Segura, M., 2011. High heat flow from Enceladus' south polar region measured using 10-600 cm^{-1} Cassini/CIRS data. J. Geo. Res. 116, E03003.

Joseph, J.H., Wiscombe, W.J., Weinman, J.A., 1976. The delta-Eddington approximation for radiative flux transfer. J. Atom. Sci. 33, 2452–2459.

Kuchiki, K., Aoki, T., Tanikawa, T., Kodama, Y., 2009. Retrieval of snow physical parameters using a ground-based spectral radiometer. Appl. Opt. 48, 5567–5582.

Labbé-Lavigne, S., Barret, S., Garet, F., Duvillaret, L., Coutaz, J.-L., 1998. Far-infrared dielectric constant of porous silicon layers measured by terahertz time-domain spectroscopy. Appl. Phys. 83, 8007–8010.

Leyrat, C., Spilker, L.J., Altobelli, N., Pilorz, S., Ferrari, C., 2008. Infrared observations of Saturn's rings by Cassini CIRS: Phase angle and local time dependence. Planet. Space. Sci. 56, 117–133.

Marouf, E.A., Tyler, G.L., Zebker, H.A., Simpson, R.A., Eshleman, V.R., 1983. Particle size distributions in Saturn's rings from Voyager 1 radio occultation. Icarus 54, 189–211.

Maxwell-Garnett, J., 1904. Colours in metal glasses and in metallic films. Phil. Trans. Roy. Soc. A203, 385–420.

Mie, G., 1908. Contributions to the optics of turbid media, particularly colloidal metal suspensions (in German). Ann. Phys. 25, 377–445.

Mishchnko, M.I., 1994. Asymmetry parameters of the phase function for densely packed scattering grains. J. Quant. Spectrosc. Radiat. Transfer 52, 95–110.

Mishima, O., Klug, O.O., Whalley, E., 1983. The far-infrared spectrum of ice Ih in the range 8-25 cm^{-1}: Sound waves and difference bands, with application to Saturn's rings. J. Chem. Phys. 78, 6399–6404.

Moersch, J.E., Christensen, P.R., 1995. Thermal emission from particulate surfaces: A comparison of scattering models with measured spectra. J. Geo. Phys. 100, 7465–7477.

Morishima, R., Salo, H., Ohtsuki, K., 2009. A multilayer model for thermal infrared emission of Saturn's rings: Basic formulation and implications for Earth-based observations. Icarus 201, 634–654.

Morishima, R., Spilker, L., Salo, H., Ohtsuki, K., Altobelli, N., Pilorz, S., 2010. A multilayer model for thermal infrared emission of Saturn's rings II: Albedo, spins, and vertical mixing of ring particles inferred from Cassini CIRS. Icarus 210, 330-345.

Morishima, R., Spilker, L., Ohtsuki, K., 2011. A multilayer model for thermal infrared emission of Saturn's rings III: Thermal inertia inferred from Cassini CIRS. Icarus 215, 107–127.

Mustard, J.F., Hays, J.E., 1997. Effects of hyper fine particles on reflectance spectra from 0.3 to 25 μm. Icarus 125, 145–163.

Nicholson, P.D. et al., 2008. A close look at Saturn's rings with Cassini VIMS. Icarus 193, 182–212.

Pitman, K.M., Wolff, M.J., Clayton, G.C., 2005. Application of modern radiative transfer tools to model laboratory quartz emissivity. J. Geo. Phys. 110, E08003.

Poulet, F., Cruikshank, D.P., Cuzzi, J.N., Roush, T.L., French, R.G., 2003. Composition of Saturn's rings A, B, and C from high resolution near-infrared spectroscopic observations. Astron. Astrophys. 412, 305–316.

Spilker, L.J., Pilorz, S.H., Edgington, S.G., Wallis, B.D., Brooks, S.M., Pearl, J.C., Flasar, F.M., 2005. Cassini CIRS observations of a roll-off in Saturn ring spectra at submillimeter wavelengths. Earth, Moon, and Planets 96, 149–163.

Spilker, L.J. et al., 2006. Cassini thermal observations of Saturn's main rings: Implications for particle rotation and vertical mixing. Planet. Space Sci. 54, 1167–1176.

Wald, A.E., 1994. Modeling thermal infrared (2-14 μm) reflectance spectra of frost and snow. J. Geo. Phys. 99, 24241–24250.

Wiscombe, W.J., 1977. The delta-M method: rapid yet accurate radiative flux calculations for strong asymmetric phase functions. J. Atom. Sci. 34, 1408–1422.

Zebker, H.A., Marouf, E.A., Tyler, G.L., 1985. Saturn's rings - Particle size distributions for thin layer model. Icarus 64, 531–548.

Figure captions

Fig. 1. Examples of β_{therm} as a function of ν, given by Eq. (9). Here we adopt $T_{\text{w1}} = 105$ K and $T_{\text{c1}} = 80$ K, and T_0 is obtained from a Planck fit (Eq. (4)). Different colors represent different values of the fraction of the warm portion, f_{w1}.

Fig. 2. Number of spectra, N_{spec}, mean solar phase angle, α, and mean absolute solar elevation angle $|B'|$ of spectrum divided in six radial bins and temperature (T_0) bins of a 5 K interval.

Fig. 3. The relative emissivity $\epsilon_{\text{rel},1}$ for the inner C ring given by Eq. (8). Different colors represent different temperature bins: 70-75 K(purple), 75-80 K(blue), 80-85(light blue), 85-90 K(brown), 90-95 K(orange), and 95-100 K (red). The upper panel shows the entire wavenumber range of the CIRS far-infrared channel, whereas the bottom panel shows the short wavenumber roll-off region. Note the difference in the vertical scales in these panels.

Fig. 4. The same with Fig. 3, but for the case of the outer B ring.

Fig. 5. The real (n) and imaginary (k) parts of refractive indices of water ice. The black solid lines represent n and k for crystalline water ice at 136 K for $\nu > 50$ cm^{-1} (Curtis et al., 2005) and k at 90 K for 10 cm^{-1} $< \nu < 30$ cm^{-1} (Mishima, 1983). n is assumed to be constant for $\nu < 50$ cm^{-1}, and $\log k$ is linearly interpolated between 30 cm^{-1} and 50 cm^{-1}. The black dashed lines represent n and k with the intra-grain porosity ϕ of 0.5. The blue lines represent n and k for amorphous water ice at 106 K (Curtis et al., 2005).

Fig. 6. Extinction efficiency, Q_{ext}, single scattering albedo, ω, and emissivity, ϵ_{model}, as a function of wavenumber calculated from the Mie theory and the Hapke's model. Different colors represent different grain sizes. In the panels of ω and ϵ_{model}, the black lines represent a size distribution case with $r_{\text{min}} = 1$ μm, $r_{\text{max}} = 1$ cm, and $p = 3$. (a) parameters calculated without diffraction removal (Q_{ext0}, ω_0, and ϵ_{model} calculated with ω_0), (b) parameters calculated with diffraction removal, and (c) parameters calculated with diffraction removal and the intra-grain porosity ϕ of 0.5. For Figs. 6a and 6b, $\phi = 0$.

Fig. 7. Contour of $\tilde{R}_2$ on the p vs. $r_{\max}$ plane. A cross represents the location of the best-fit values where $\tilde{R}_2 = 0$.

Fig. 8. Emissivities from observations ϵ_1 (blue) and ϵ_2 (black) and modeled emissivity ϵ_{model} (red) with the best fitted $r_{\max}$ and p (shown in the parenthesis) for the inner C ring, the outer B ring, the Cassini division, and the A ring. For each ring, one high temperature case and one low temperature case are shown. The fitted temperatures and the fraction of the warm portion are shown in the panels.

Fig. 9. Estimated p and $r_{\max}$ for all temperatures and all rings.

Fig. 10. Effective radius r_{eff} (Eq. (29)) and median radius r_{med} (Eq. (31)) calculated from p and $r_{\max}$ in Fig. 9.

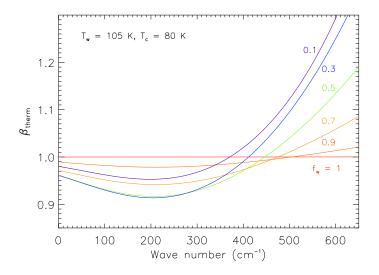$T_w = 105$ K, $T_c = 80$ K

0.1

0.3

0.5
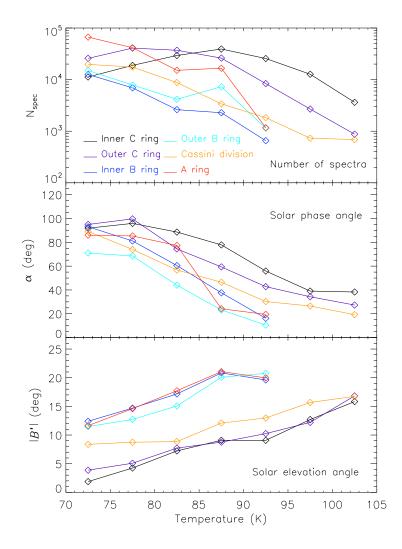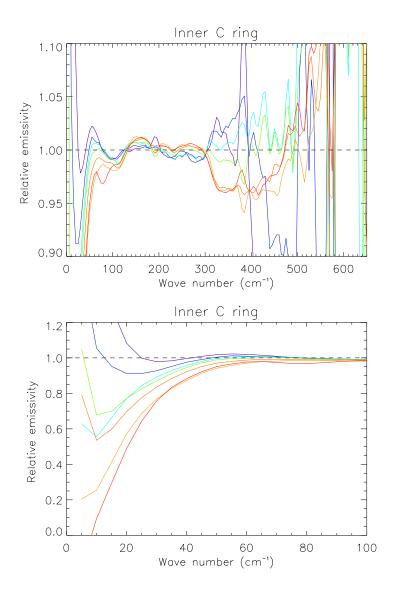
0.7

0.9

$f_w = 1$

β_{therm}

Wave number (cm^{-1})

Fig. 1.

Fig. 2.

Fig. 3.

Fig. 4.

31

Fig. 5.

(a) With diffraction

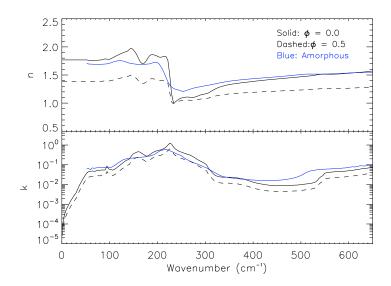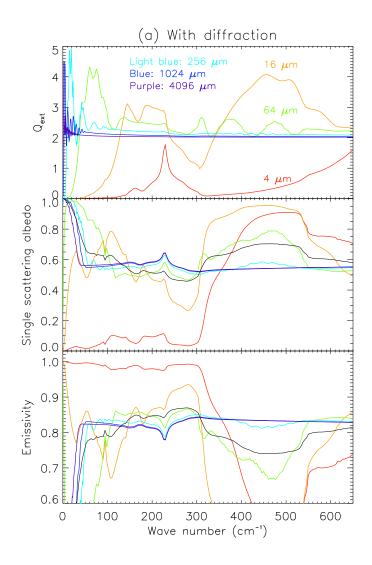Light blue: 256 μm
Blue: 1024 μm
Purple: 4096 μm

16 μm

64 μm

4 μm
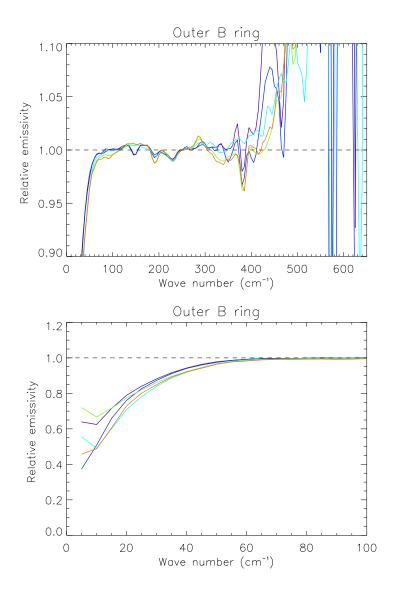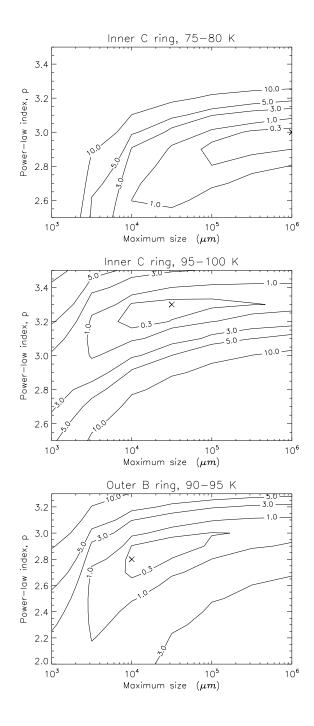
Fig. 6.
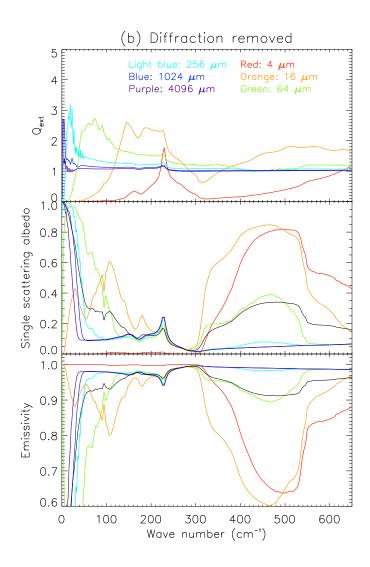
Fig. 6. -continue

Fig. 6. -continue

35

Inner C ring, 75–80 K

Inner C ring, 95–100 K

Outer B ring, 90–95 K

Fig. 7.

Inner C ring, 75–80 K

Red : $\epsilon_{model}(r_{max}=10^{6.0}\ \mu m,\ p=3.00)$
Black: ϵ_2
Blue: ϵ_1

$T_{c1} = 77.9\ K$ $T_{c2} = 75.9\ K$
$T_{w1} = --$ $T_{w2} = 85.9\ K$
$f_{w1} = 0.000$ $f_{w2} = 0.095$

Emissivity

Wave number (cm^{-1})

Inner C ring, 95–100 K

Red : $\epsilon_{model}(r_{max}=10^{4.5}\ \mu m,\ p=3.30)$
Black: ϵ_2
Blue: ϵ_1

$T_{c1} = 97.0\ K$ $T_{c2} = 91.1\ K$
$T_{w1} = --$ $T_{w2} = 133.3\ K$
$f_{w1} = 0.000$ $f_{w2} = 0.049$

Emissivity

Wave number (cm^{-1})

Fig. 8.

Outer B ring, 75−80 K

Red : $\epsilon_{model}(r_{max}=10^{4.5}\ \mu m,\ p=2.90)$
Black: ϵ_2
Blue: ϵ_1

$T_{c1} = 75.1$ K $T_{c2} = 69.0$ K
$T_{w1} = 100.1$ K $T_{w2} = 87.0$ K
$f_{w1} = 0.033$ $f_{w2} = 0.256$

Outer B ring, 90−95 K

Red : $\epsilon_{model}(r_{max}=10^{4.0}\ \mu m,\ p=2.80)$
Black: ϵ_2
Blue: ϵ_1

$T_{c1} = 87.9$ K $T_{c2} = 86.1$ K
$T_{w1} = 108.7$ K $T_{w2} = 119.9$ K
$f_{w1} = 0.090$ $f_{w2} = 0.059$

Fig. 8. -continue

Fig. 8. -continue

A ring, 75–80 K

Red : $\epsilon_{model}(r_{max}=10^{4.5}\ \mu m,\ p=2.90)$
Black: ϵ_2
Blue: ϵ_1

$T_{c1} = 74.8$ K $T_{c2} = 74.0$ K
$T_{w1} = 84.8$ K $T_{w2} = 99.3$ K
$f_{w1} = 0.199$ $f_{w2} = 0.054$

A ring, 90–95 K

Red : $\epsilon_{model}(r_{max}=10^{4.0}\ \mu m,\ p=2.90)$
Black: ϵ_2
Blue: ϵ_1

$T_{c1} = 90.7$ K $T_{c2} = 85.7$ K
$T_{w1} = --$ $T_{w2} = 113.6$ K
$f_{w1} = 0.000$ $f_{w2} = 0.082$

Fig. 8. -continue

Fig. 9.

Fig. 10.